

In-Flight Performance of SPIDER's 280 GHz Receivers

E. C. Shaw^{a,b,c}, P. A. R. Ade^d, S. Akers^e, M. Amiri^f, J. Austermann^g, J. Beall^g, D. T. Becker^g, S. J. Benton^h, A. S. Bergman^h, J. J. Bock^{i,j}, J. R. Bond^k, S. A. Bryan^l, H. C. Chiang^{m,n}, C. R. Contaldi^o, R. S. Domagalski^p, O. Doré^{i,j}, S. M. Duff^g, A. J. Duivenvoorden^{q,h}, H. K. Eriksen^r, M. Farhang^s, J. P. Filippini^c, L. M. Fissel^t, A. A. Fraisse^h, K. Freese^{a,b,u}, M. Galloway^r, A. E. Gambrel^v, N. N. Gandilo^w, K. Ganga^x, S. M. Gibbs^c, S. Gourapura^h, A. Grigorian^g, R. Gualtieri^{c,y}, J. E. Gudmundsson^{z,u}, M. Halpern^f, J. Hartley^p, M. Hasselfield^l, G. Hilton^g, W. Holmes^j, V. V. Hristovⁱ, Z. Huang^k, J. Hubmayr^g, K. D. Irwin^{2,3}, W. C. Jones^h, A. Kahn^c, Z. D. Kermish^h, C. King^e, C. L. Kuo², A. R. Lennox^c, J. S.-Y. Leung^{p,4}, S. Li^{h,5}, T. V. Luu^h, P. V. Masonⁱ, J. May^e, K. Megerian^j, L. Moncelsiⁱ, T. A. Morfordⁱ, J. M. Nagy^e, R. Nie^c, C. B. Netterfield^{p,6}, M. Nolta^k, B. Osherson^c, I. L. Padilla^{e,p,7}, A. S. Rahlin^{s,v}, S. Redmond^{i,j}, C. Reintsema^g, L. J. Romualdez⁹, J. E. Ruhl^e, M. C. Runyan^j, J. A. Shariff^k, C. Shiu^h, J. D. Soler¹⁰, X. Song^h, S. Tartakovsky^h, H. Thommesen^r, A. Trangsrud^{i,j}, C. Tucker^d, R. S. Tuckerⁱ, A. D. Turner^j, J. Ullom^g, J. F. van der List^h, J. Van Lanen^g, M. R. Visser^g, A. C. Weber^j, I. K. Wehus^r, S. Wen^e, D. V. Wiebe^f, and E. Y. Young^{2,3}

^aDepartment of Physics, The University of Texas at Austin, Austin, TX 78712, USA

^bWeinberg Institute for Theoretical Physics, Texas Center for Cosmology and Astroparticle Physics, Austin, TX 78712, USA

^cDepartment of Physics, University of Illinois Urbana-Champaign, 1110 W Green St, Urbana, IL 61801, USA

^dSchool of Physics and Astronomy, Cardiff University, Cardiff CF24 3AA, UK

^eDepartment of Physics, Case Western Reserve University, 10900 Euclid Ave, Cleveland, OH 44106, USA

^fDepartment of Physics and Astronomy, University of British Columbia, Vancouver, BC V6T 1Z1, Canada

^gNational Institute of Standards and Technology, 325 Broadway Mailcode 817.03, Boulder, CO 80305, USA

^hDepartment of Physics, Princeton University, Jadwin Hall, Princeton, NJ 08544, USA

ⁱDivision of Physics, Mathematics and Astronomy, California Institute of Technology, Pasadena, CA 91125, USA

^jJet Propulsion Laboratory, Pasadena, CA 91011, USA

^kCanadian Institute for Theoretical Astrophysics, University of Toronto, Toronto, ON M5S 3H4, Canada

^lSchool of Earth and Space Exploration, Arizona State University, Tempe, AZ 85283, USA

^mDepartment of Physics, McGill University, Montreal, QC H3A 2T8, Canada

ⁿSchool of Mathematics, Statistics and Computer Science, University of KwaZulu-Natal, Durban, South Africa

^oBlackett Laboratory, Imperial College London, London SW7 2AZ, UK

^pDepartment of Astronomy and Astrophysics, University of Toronto, Toronto, ON M5S 3H4, Canada

^qCenter for Computational Astrophysics, Flatiron Institute, New York, NY 10010, USA

^rInstitute of Theoretical Astrophysics, University of Oslo, NO-0315 Oslo, Norway

^sDepartment of Physics, Shahid Beheshti University, 1983969411, Tehran Iran

^tDepartment of Physics, Engineering Physics and Astronomy, Queen’s University, Kingston, ON K7L 3N6, Canada

^uThe Oskar Klein Centre for Cosmoparticle Physics, Department of Physics, Stockholm University, AlbaNova, SE-106 91 Stockholm, Sweden

^vKavli Institute for Cosmological Physics, University of Chicago, Chicago, IL 60637, USA

^wSteward Observatory, Tuscon, AZ 85721, USA

^xUniversité de Paris, CNRS, AstroParticule et Cosmologie, F-75013 Paris, France

^yDepartment of Physics and Astronomy, Northwestern University, Evanston, IL 60208, USA

^zScience Institute, University of Iceland, 107 Reykjavik, Iceland

¹Department of Astronomy and Astrophysics, Pennsylvania State University, University Park, PA 16802, USA

²Department of Physics, Stanford University, Stanford, CA 94305, USA

³SLAC National Accelerator Laboratory, Menlo Park, CA 94025, USA

⁴Dunlap Institute for Astronomy and Astrophysics, University of Toronto, Toronto, ON M5S 3H4, Canada

⁵Department of Mechanical and Aerospace Engineering, Princeton University, Engineering Quadrangle, Princeton, NJ 08544, USA

⁶Department of Physics, University of Toronto, Toronto, ON M5S 3H4, Canada

⁷Department of Physics and Astronomy, Johns Hopkins University, Baltimore, MD 21218, USA

⁸Department of Astronomy and Astrophysics, University of Chicago, Chicago, IL 60637, USA

⁹University of Toronto Institute for Aerospace Studies, Toronto, ON M5S 3H4, Canada

¹⁰Max-Planck-Institute for Astronomy, Königstuhl 17, 69117, Heidelberg, Germany

ABSTRACT

SPIDER is a balloon-borne instrument designed to map the cosmic microwave background at degree-angular scales in the presence of Galactic foregrounds. SPIDER has mapped a large sky area in the Southern Hemisphere using more than 2000 transition-edge sensors (TESs) during two NASA Long Duration Balloon flights above the Antarctic continent. During its first flight in January 2015, SPIDER observed in the 95 GHz and 150 GHz frequency bands, setting constraints on the B-mode signature of primordial gravitational waves. Its second flight in the 2022-23 season added new receivers at 280 GHz, each using an array of TESs coupled to the sky through feedhorns formed from stacks of silicon wafers. These receivers are optimized to produce deep maps of polarized Galactic dust emission over a large sky area, providing a unique data set with lasting value to the field. In this work, we describe the instrument’s performance during SPIDER’s second flight.

Keywords: SPIDER, cosmic microwave background, feedhorn coupled transition-edge sensors, scientific ballooning, 280 GHz cosmology

1. INTRODUCTION

SPIDER is a balloon-borne instrument specifically designed to advance the search for the inflationary signature of primordial gravitational waves in the B -mode polarization of the cosmic microwave background (CMB) in the presence of Galactic foregrounds.¹⁻⁴ The inflationary B -mode polarization signal is expected to be extremely faint, with anisotropies $\ll 1 \mu\text{K}$. Experimental detection of such a signal requires extremely sensitive detectors, tight control over polarized instrumental systematics, and effective strategies to mitigate the effects from atmospheric and Galactic sources. Earth’s millimeter-wave absorptive and emissive atmosphere attenuates the CMB signal, increases optical loading, and produces fake signals from fluctuations in atmospheric brightness. The two primary sources of Galactic foreground polarization, synchrotron radiation and thermal emission from dust, overshadow

E-mail: elle.shaw@utexas.edu

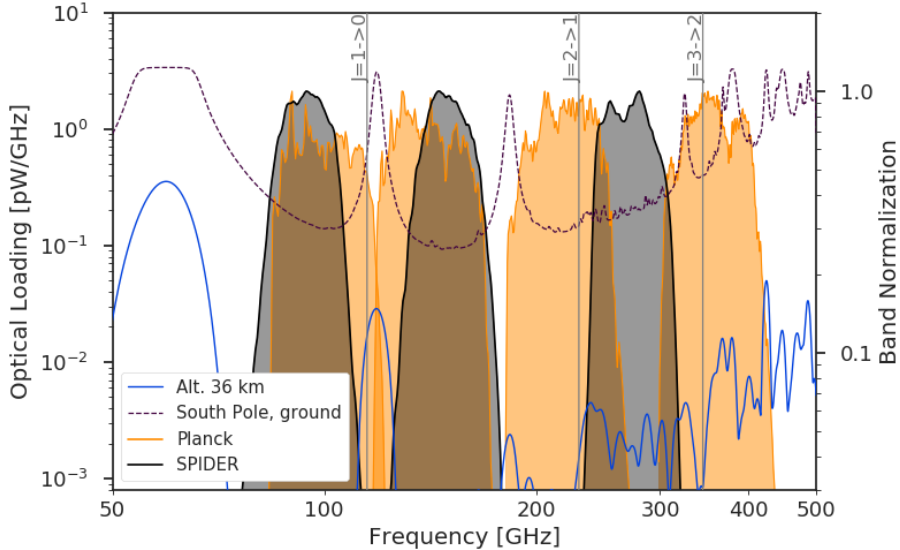


Figure 1: *Planck* (orange) and SPIDER’s (black) bandpasses superimposed over the optical loading from the atmosphere at the South Pole (dash) and at 36 km altitude (blue). Rotational transition spectral lines for Galactic CO are also shown. SPIDER’s 280 GHz band provides an independent measurement of polarized Galactic dust emission at frequencies that are difficult to access from the ground.

the polarized CMB signals at all frequencies when the brightness is averaged across the full sky.⁵ Even away from the Galactic plane in relatively ‘clean’ regions of sky, the diffuse thermal dust emission is significant and requires proper characterization to distinguish from any CMB signal. The isolation of CMB signals from foregrounds requires high-quality observations in multiple frequency bands, where the different spectral behaviors of each component can, in principle, be leveraged to separate them.

SPIDER’s mission is to set an upper limit on the tensor-to-scalar ratio, r , at the few-percent level while producing high-quality maps of polarized Galactic dust emission. SPIDER has mapped the polarization of the millimeter sky in three frequency bands centered near 95 GHz, 150 GHz, and 280 GHz during two NASA Long Duration Balloon (LDB) flights above the Antarctic continent. At an altitude of ~ 35 km, the ballooning platform allows for observations over a wide sky area with minimal contamination from atmospheric emission. Under such conditions, we can maximize detector sensitivity to make high-fidelity maps in a matter of days.

The detailed shape of SPIDER’s bands is shown in Figure 1, together with the polarized bands of the *Planck* High Frequency Instrument. Atmospheric loading brightness for observation locations at the South Pole and at an altitude of 36 km is superimposed on the frequency bands, showing the placement of SPIDER’s observation bands between absorption lines. SPIDER’s 280 GHz band complements the 95 and 150 GHz data sets by providing high-contrast dust maps with a shorter lever arm than the *Planck* 353 GHz band to extrapolate dust models to lower frequencies. Moreover, the SPIDER 280 GHz receivers are vastly more sensitive than any prior receiver in this band. Maps from SPIDER’s 280 GHz receivers will improve the analysis of the combined SPIDER data set^{6,7} and benefit the larger community exploring the CMB and modeling Galactic dust.

In January 2015, SPIDER completed its first flight from the LDB Facility at McMurdo Station, Antarctica. For clarity, we refer to this flight as ‘SPIDER-1’. During a 16-day flight, SPIDER-1 mapped approximately 10% of the sky with three receivers tuned to 95 GHz and three to 150 GHz. The large sky area allows us to sample the angular power spectrum over a wide range of multipoles, $35 \lesssim \ell \lesssim 250$, covering the relevant multipole range for the expected peak in the primordial B -mode signal near $\ell \sim 80$. SPIDER-2 is the second flight of the SPIDER experiment, which targeted the same sky region during another 16-day flight in December 2022 – January 2023. The second flight redeployed three SPIDER-1 receivers (two at 95 GHz and one at 150 GHz) and incorporated

three novel 280 GHz receivers. In these proceedings, we briefly summarize the SPIDER-2 instrument and 280 GHz receiver design, describe the final optical filtering configuration selected for flight, and discuss the receivers' in-flight optical loading and noise performance.



(a) SPIDER-1 January 1, 2015

(b) SPIDER-2 December 22, 2023

Figure 2: Photos of the fully integrated SPIDER-1 and SPIDER-2 payloads before their respective launches. Some key components visible in the photographs are the solar panels, star cameras, electronics, telescope forebaffles, and the sunshield. SPIDER-1 photo from Jon Gudmundsson.

2. SPIDER-2 INSTRUMENT

2.1 Payload

The SPIDER-2 instrument builds on the heritage of SPIDER-1, using a similar design and reusing much of the same electronics and hardware – the visual similarities are evident in pre-flight photos shown in Figure 2. The design choices of the SPIDER-1 instrument and receivers have been well described in several previous publications (Refs. 8–12). For both payloads, a massive ~ 1300 L liquid helium cryostat houses the six receivers. Inside the cryostat, the main tank provides 4 K cooling power to the telescope receivers and the cryogenic half-wave plates (HWP). Closed-cycle helium-3 sorption refrigerators inside each receiver cool the focal planes and detector assemblies to their 300 mK operating temperatures. A 20 L superfluid tank (SFT) is filled continuously from the main tank through capillaries, and it cools the telescopes' internal optical baffling and sub-Kelvin refrigerators to 1.6 K. Helium vapor from the main tank passes through heat exchangers on two stages of vapor-cooled shields, VCS1 and VCS2, cooling the shields and a series of filters mounted at each stage. In-flight VCS1 hovers around 35 K and VCS2 around 110 K.

The cryostat rests on a lightweight carbon fiber and aluminum gondola surrounded by an aluminized Mylar sunshield. Forebaffles extending from the telescope apertures shield the detectors from glinting off the Earth's surface and from polarized reflections from the balloon.¹¹ A solar panel array provides 2 kW of continuous power to the payload. The instrument is scanned in elevation using dual linear actuators and is scanned in azimuth

using a reaction wheel and pivot motor. The gondola features pin-hole sun sensors, an upgraded gyroscope, a magnetometer, and a dual-boresight star camera system to provide in-flight pointing control and post-flight pointing reconstruction. The gondola frame, sunshield, and solar panels were entirely rebuilt for the second flight, with several changes to the overall design to reduce mass and improve strength. Details on the changes and updates to the SPIDER-2 gondola and sunshield can be found in Refs. 13, 14. A new flight cryostat, based on the previous design,¹⁵ was manufactured at Meyer Tool*, and included a larger liquid helium tank that demonstrated improved vacuum performance pre-flight relative to the original unit. Refs. 16, 17 report on the integration and pre-flight testing of the SPIDER-2 cryostat.

2.2 280 GHz Receivers

The SPIDER receivers are small-aperture, two-lens, refracting telescopes designed with an emphasis on reducing the internal loading, or the thermal emission, of the inside of the instrument. Figure 3 shows a photograph and a cutaway drawing of a 280 GHz receiver (the optical chain elements skyward of the receivers are not pictured). SPIDER’s three 280 GHz telescopes were constructed from decommissioned 95 and 150 GHz receivers and are outfitted with new focal planes and optics. The 280 GHz receiver design and pre-flight characterization were described in previous SPIE proceedings (Ref. 18), with more details included in Ref. 19. The following subsections provide a brief overview, and we comment on changes made to the optical stacks since Shaw et al. 2020.¹⁸

2.2.1 Detectors

The 280 GHz detector arrays are feedhorn-coupled transition-edge sensor (TES) arrays developed and fabricated at NIST.²⁰ The detector arrays and sub-Kelvin readout electronics are housed inside each receiver’s focal plane unit (FPU) and operate at 300 mK. SPIDER’s TES bolometers are tailored to take advantage of extremely low background loading in the space-like flight environment, and a TES designed for flight conditions easily saturates during lab testing. Every SPIDER bolometer has two TESs with different superconducting critical temperatures, T_c , connected in series to address this issue. An aluminum manganese (AlMn) TES ($T_c \sim 450$ mK) provides low noise for science data acquisitions on the 280 GHz detectors, and an aluminum TES with higher T_c (~ 1.6 K) extends the bolometer dynamic range for the higher optical loading conditions of lab-based measurements. Shunt resistors with $\sim 1/10$ of the science TESs operational resistance are connected in parallel with the TESs, providing a strong voltage bias. The TESs are read out using a three-stage time-division multiplexed Superconducting QUantum Interference Device (SQUID) system designed at NIST.²¹ Multi-Channel Electronics (MCE) developed at the University of British Columbia control the SQUID readout.²² When the receivers are referenced individually, they are called by their FPU naming convention: “Y3”, “Y4b”, and “Y5”.

2.2.2 Receiver Optics and Filtering

The detectors and focal plane array are located at the center of the receivers, which mount to the base of the main (4 K) helium tank and extend up through cylindrical ports. The two high-density polyethylene lenses are cooled to 4 K to reduce in-band loading from dielectric loss in the plastic. An optical baffle surrounding the optical path between the lenses and a magnetic shield surrounding the focal plane are cooled to 2 K. The optical baffle is blackened to absorb sidelobe power falling outside the optical stop (270 mm diameter), which sits at the top of the baffle.^{8,9}

The single-axis symmetry of the telescopes is beneficial for reducing polarized instrumental systematics that could show up in the data as false sky signals. A monochromatic half-wave plate (HWP) provides polarization modulation to mitigate beam systematics and increase polarization coverage. The 280 GHz HWPs are 1.66 mm thick birefringent sapphires from Rubicon Technology[†] with a ~ 0.125 mm Cirlex AR coat.^{23,24} The HWPs are mounted to the main helium tank directly skyward of the receivers and are rotated twice per sidereal day in multiples of 22.5 degrees.

We utilize a combination of carefully positioned filters to reflect out-of-band radiation while minimizing the in-band thermal radiation of the filters themselves. The optical stack includes thin reflective metal mesh shaders,²⁵ multi-layered hot-pressed metal-mesh low-pass filters,²⁶ and thicker dielectric filters that shape the

*Meyer Tool & Mfg, Oak Lawn, IL.

†Rubicon Technology, Bensenville, IL.

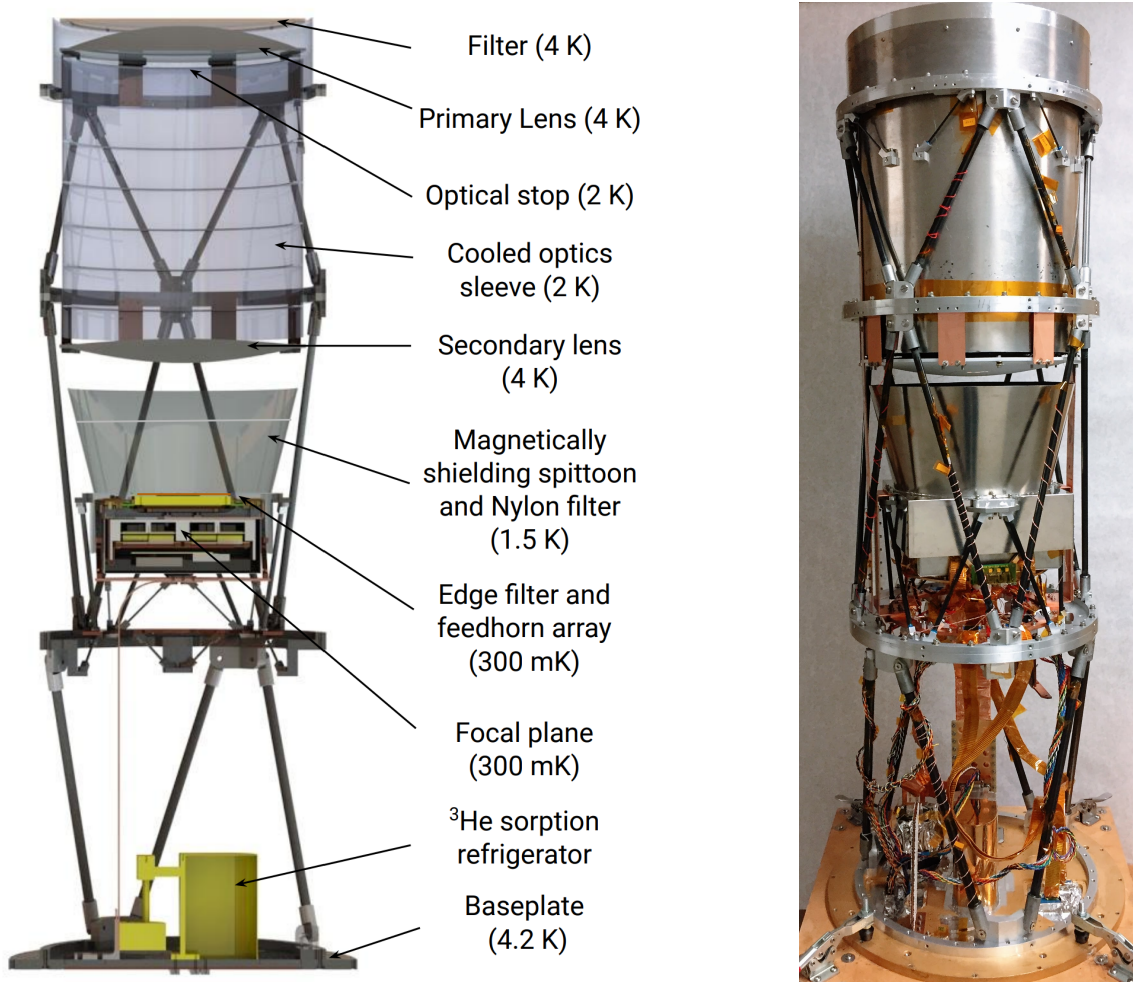


Figure 3: (Left): A simplified cutaway CAD model of the SPIDER-2 280 GHz receivers, including the optics, cold baffling systems, filters, focal plane, and ³He sorption refrigerator. The rest of the optical stack skyward of the receivers, including the half-wave plate, filters, and vacuum window, are not pictured in the diagram. (Right): A fully integrated 280 GHz receiver. Before installation into a cryostat, the telescope is wrapped in copper-clad G-10 and taped at the seams to be light-tight. The 280 GHz receivers stand approximately 1.2 m (~ 47 in) tall when measured from the top of the base plate to the top of the 4K filter stack. Figure adapted from Shaw et al. 2020 with permission.¹⁸

desired bandpass. The original optics and filtering scheme for the 280 GHz receivers was detailed in Ref. 18. In that scheme, two reflective IR “shaders” mounted directly below the 1/16” thick ultra-high molecular weight polyethylene vacuum window provide the first defense against infrared radiation. Additional shaders are mounted at both VCS stages with two metal-mesh low-pass filters mounted beneath them on the ~ 35 K VCS stage. Another 12 cm^{-1} (360 GHz) cutoff filter is mounted at 4 K just skyward of the primary lens and underneath the sapphire HWP. A 3/32” AR-coated nylon filter is located in the 1.6 K magnetic shield spittoon aperture to absorb additional infrared radiation.²⁷ Finally, the high-frequency edge of the 280 GHz bandpass is defined by a 10.5 cm^{-1} (~ 315 GHz) low-pass metal-mesh filter mounted at 300 mK, directly above the feedhorn array.

Before flight, we had concerns about high internal loading, but we were limited in our ability to measure it under comparable flight-loading environments. Laboratory tests suggested that the metal-mesh low-pass filters at the 35 K VCS stage were running warmer than desired, and we worried that their emissivity contributed to high loading measurements. We made precautionary changes to the optical stacks to balance a reduction in loading

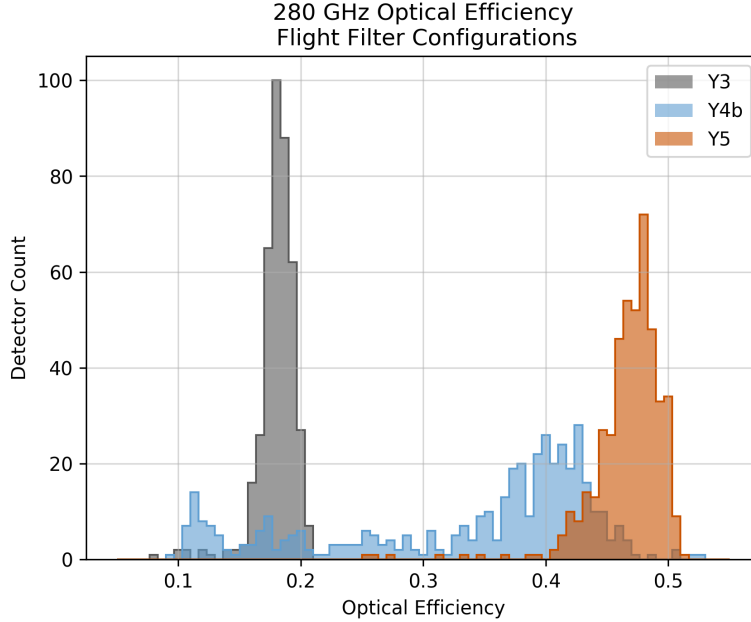


Figure 4: Histogram of optical efficiency from the flight filter configuration. All receivers have a second sapphire filter, and Y3 has an additional NDF. These optical efficiencies are derived assuming an ideal detector efficiency of $0.871 \text{ pW/K}_{\text{RJ}}$ (a top hat bandwidth of 63 GHz). The tail of lower efficiency detectors on Y4b is due to defects in the feedhorn array.

while conserving optical efficiency to the greatest possible extent. The low in-band absorption loss and high thermal conductivity of sapphire are ideal for an IR filter. So, we moved all IR shaders to the warmer VCS stage and installed sapphire filters in front of the metal mesh filters. The intention was that the sapphire filters, similar to an alumina filter, would conduct the IR power load onto the VCS shields rather than re-radiate onto the emissive (and less conductive) filters behind. Due to pre-deployment time constraints and what was commercially available immediately, the additional sapphire filters are the same materials as the 280 GHz HWPs. Notably, the additional sapphire filters decreased detector responsivity by less than 5%.

One of the FPUs, Y3, has lower saturation power than the other two. So, we implemented a 2 K neutral density filter (NDF) on Y3 to ensure that we would have at least one fully functional 280 GHz FPU. The selected NDF was constructed from four laminated 0.03" sheets of carbon black-filled polyethylene, measured to have $\sim 42\%$ transmission. The 280 GHz detector optical efficiencies measured before flight are presented in Figure 4. With the additional sapphire filter, the bulk of Y5's detectors are around 47% efficient, and the higher optical efficiency detectors on Y4b cluster around 40%. The additional NDF on Y3 reduces the optical efficiency to $\sim 18\%$. For a more detailed discussion of pre-flight characterization and the filtering configuration chosen for the flight, please refer to Ref. 19.

3. 2022-2023 FLIGHT

The SPIDER-2 payload launched on December 22, 2022, at 10:26 AM NZDT. The payload circumnavigated the continent at an average altitude of 35 km for 16 days. The payload hovered over the Transantarctic Mountain range for several days and was terminated on January 7, 2023, near Hercules Dome, Antarctica. Figure 5a shows the payload flight path over the Antarctic continent alongside the SPIDER-1 flight path in 2015. Both flights' longitude, latitude, and altitude profiles are shown in Figure 5b. Within three weeks of flight termination, the data drives and payload hardware were fully recovered with assistance from Kenn Borek Air and South Pole Station personnel.

The majority of the payload subsystems operated as designed throughout the flight. All power, pointing, thermal management, detector monitoring, and half-wave plate rotation systems operated successfully. Addition-

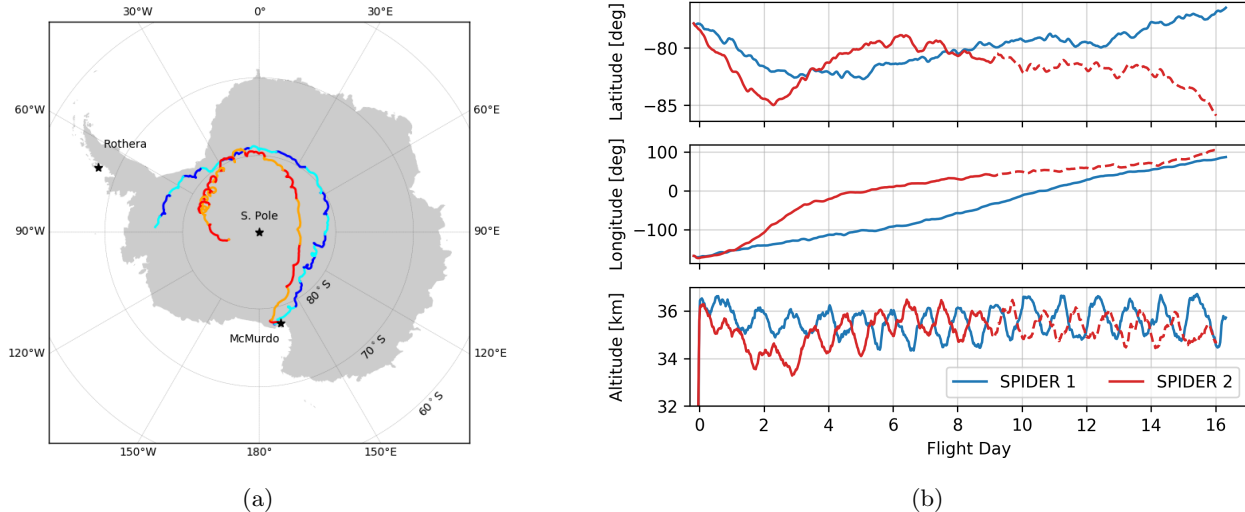


Figure 5: (*Left*): Flight trajectory during SPIDER’s flights. SPIDER-1 in blue/cyan, and SPIDER-2 in red/orange. Alternating colors along each track denote days. (*Right*): Payload longitude (top), latitude (middle), and altitude (bottom) during SPIDER’s flights. $T=0$ marks when the payloads reached an altitude of 36 km. The solid lines on SPIDER-2 data correspond to the nominal science observation period.

ally, all of SPIDER’s receivers performed exceptionally well, as discussed below. The flight nonetheless suffered several challenges, partially due to the tight schedule and logistical constraints of the 2022-23 season. We were not able to fill the liquid helium tank to full capacity before launch, so science data collection ceased on the ninth day of flight after the tanks emptied. We also found evidence after launch of a helium leak into the vacuum space (similar to SPIDER-1¹⁵). Finally, the payload’s star cameras did not function at float, so we relied on the remaining pointing sensors for attitude control. Given SPIDER’s relatively modest pointing requirements, however, we expect to be able to adequately reconstruct a pointing solution using the other pointing sensors on the gondola (sun sensors, magnetometer, gyroscopes) and via cross-correlation between *Planck* temperature maps and SPIDER’s own data. Significant progress has been made on this iterative process toward science-quality maps.

4. IN-FLIGHT OPTICAL LOADING

The radiative power absorbed by the detectors in flight (“optical loading”) is a critical performance parameter due to its effect on instrumental noise. We extract a measurement of the optical loading on the detectors in the near-space environment by comparing load (IV) curves taken at float to those taken during pre-flight dark testing (corrected for slight focal plane temperature differences). This comparison yields direct estimates of the power absorbed by each detector.

The distribution of in-flight absorbed power, P_{opt} , for all 280 GHz detectors is shown in Figure 6a. The loading reported for each detector is the average of 4–5 load curves taken in the first 24 hours at float. The median absorbed power measured on Y3, Y4b, and Y5 is 0.6, 1.6, and 1.9 pW, respectively. These powers are well clear of saturation for all detectors; the absorbed powers on Y5 detectors are just above half their saturation powers, while Y3 and Y4b are less. For SPIDER’s 280 GHz receivers, the CMB and atmosphere are only a small contribution to the total absorbed power; even for Y5, the 280 GHz receiver with the highest optical efficiency, their combined contribution is expected to be less than 0.12 pW.¹⁷

The power absorbed by each detector heavily depends on its optical efficiency (Figure 4). We can alternatively express the loading as an apparent aperture temperature, T_{inc} , by dividing P_{opt} by the detector responsivity. T_{inc} represents the in-band thermal load of everything skyward of the focal plane (optics, filters, window, baffles, atmosphere, and CMB), treated as if it originated at the aperture. Histograms of T_{inc} are presented in Figure 6b. The aperture temperatures seen by Y4b and Y5 are consistent with ~ 4.8 KRJ; this behavior was anticipated

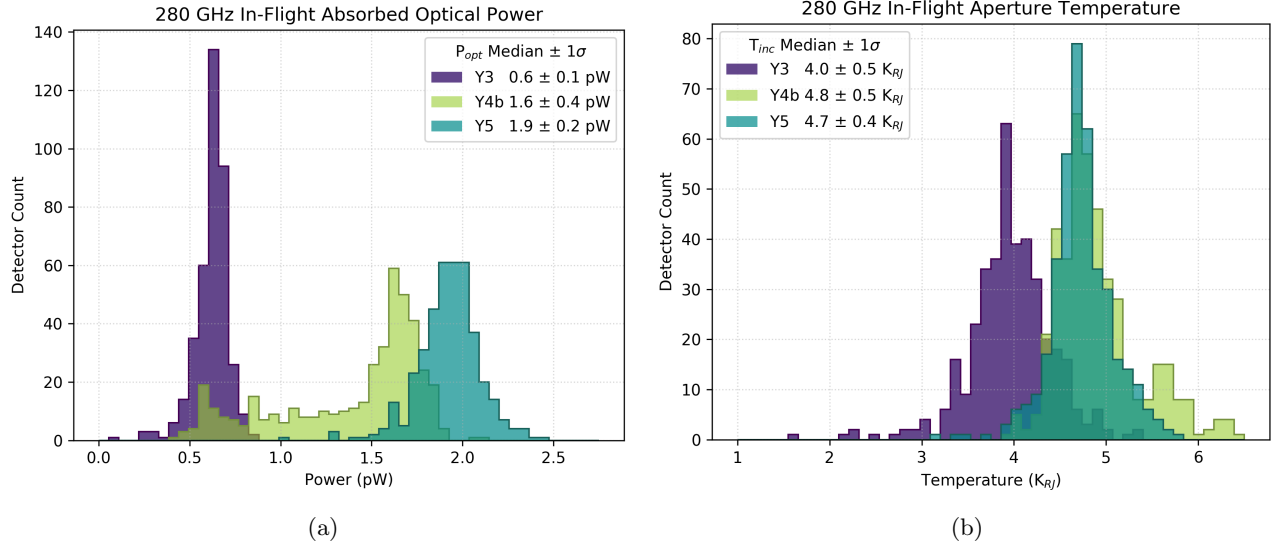


Figure 6: 280 GHz in-flight loading averages with detector data grouped by FPU. (*Left*): Absorbed optical power (*Right*): Apparent aperture temperature, including sky and internal loading, calibrated using detector responsivity.

because Y4b and Y5 have nominally identical filter stacks. The loading measured by Y3 is closer to $3.9 K_{RJ}$, presumably reduced by the effects of the NDF installed at the 2 K stage.

We can further explore to what extent detector loading varies throughout the flight. For SPIDER-1, loading variations were primarily associated with fluctuations in the FPU temperatures between fridge cycles and were on the order of 10% of the total optical loading of ~ 0.3 pW at 150 GHz.²⁸ SPIDER-2 saw substantially larger temperature fluctuations in the temperatures of its cryogenic stages and associated optical elements. Thermometer readings on the first ~ 35 K VCS stage varied between 20 and 45 K, primarily due to hysteresis in the helium boil-off flow from the main LHe tank vent. The thermometers on the second VCS stage (~ 110 K) showed a ~ 5 K oscillation. A thermistor attached to the window clamp on the Y4b aperture dropped from 270 K to 240 K in under 24 hours after reaching float altitude, then subsequently oscillated between 240–245 K during the diurnal cycles (This behavior is not necessarily unlike SPIDER-1). We must thus consider the loading variations that might result from these temperature changes.

To estimate the loading variations, we compare load curves taken on Y4b in the first 24 hours of flight to one taken later in the flight, shortly after a fridge cycle when the VCS temperatures are at a minimum. The difference in absorbed power is near 0.15 pW for the higher optical efficiency detectors on Y4b ($\Delta T_{inc} \sim 0.4 K_{RJ}$). With 0.15 pW as a lower limit on the range of loading fluctuations for the higher optical efficiency detectors, we expect the photon noise levels to fluctuate by 5% over the temperature oscillation period, representing a $\sim 5\%$ cost in mapping speed.

5. NOISE PERFORMANCE

In this section, we present initial studies of the white noise performance of the 280 GHz detectors throughout SPIDER’s second flight. Note that the analysis of this data set is still in its early stages: data cleaning is still being finalized, and sky maps are not yet mature enough to calibrate detector data against sky signals. We can nonetheless make initial estimates of noise performance, focusing in particular on periods in which the payload is not scanning, and give an approximate calibration to on-sky sensitivity based upon laboratory calibration measurements and load curves acquired during flight.

5.1 Calibration

We calibrate raw detector time streams to current, I , based on a linearized model of TES response. The calibrated TES I is derived using measurements of the detector shunt resistance, readout wire resistance, and other readout parameters. We can assess the calibration from the superconducting slope of calibrated IV curves; the superconducting slope should equal unity for a well-calibrated current. From inspections of IV curves, we expect the error due to our current calibration to be less than 1.5% for all detectors.

To express detector noise in units of equivalent absorbed power (the noise equivalent power, or NEP), we must calibrate time-ordered data from current to power. We approximate the TES responsivity, s_I , defined as the change in TES current for a small change in optical power dissipated on the bolometer island, using the responsivity equation derived in Irwin & Hilton (2005), evaluated at the zero-frequency limit,²⁹

$$s_I(\omega = 0) = -\frac{1}{IR} \left(\frac{L}{\tau_{el} R \mathcal{L}_I} + \left(1 - \frac{R_{sh}}{R} \right) \right)^{-1}, \quad (1)$$

where R and I are the TES resistance and current, R_{sh} is a shunt resistor connected in parallel to the TES, L is the TES loop inductance, \mathcal{L}_I is the TES loop gain, and τ_{el} is the TES electrical time constant. In the limit of high loop gain, the calibration factor we require reduces to the following:

$$\frac{dP}{dI} = s_I^{-1}(\omega = 0) \approx -I(R - R_{sh}). \quad (2)$$

We use Equation (2) to convert from TES current to absorbed power, then inflate the results by 6% to account for the estimated effect of finite loop gain. We use load curves acquired in the middle of the stop mode data set to derive values of TES current and resistance at the appropriate voltage bias for each data point. This method assumes that the optical loading is constant throughout the dataset. In practice, we know that the absorbed optical power on the higher optical efficiency detectors can fluctuate by at least 0.15 pW throughout flight due to the variation in cryostat temperatures.¹⁹ To bracket the error introduced by the choice of reference load curve, we repeated the noise analysis on Y4b, calibrating with a load curve taken later in flight while the cryostat’s vapor-cooled shields were at their coldest. The resulting decrease in mean Y4b detector NEP is less than 0.2%, suggesting this calibration error is negligible.

Finally, we use laboratory measurements of optical response to calibrate from NEP to NET_{CMB} , or noise-equivalent temperature, representing the detector sensitivity to the CMB signal. To calculate NET we divide NEP by dP/dT_{CMB} , computed in the small-bandwidth approximation as follows:

$$\frac{dP}{dT_{\text{CMB}}} = \frac{d}{dT_{\text{CMB}}} \left(\sqrt{2} \int d\nu \eta B(\nu, T) dA d\Omega \right) \quad (3)$$

$$\approx \sqrt{2} \frac{dP}{dT} \frac{x^2 e^x}{(e^x - 1)^2}, \quad x = \frac{h\nu_0}{k_B T_{\text{CMB}}}. \quad (4)$$

Here dP/dT is the optical responsivity (in the Rayleigh-Jeans limit) measured in the laboratory for each detector, ν_0 is the band center and the factor of $\sqrt{2}$ is included to convert the NET from units of $\sqrt{\text{Hz}}^{-1}$ to $\sqrt{\text{s}}$. We use array-averaged band centers ν_0 : 274.7 GHz, 275.0 GHz, and 269.0 GHz for Y3, Y4b, and Y5 respectively. The band centers for Y3 and Y5 are the averages of Fourier transform spectroscopy measurements.¹⁶ The measured band centers showed a 1σ spread around these medians of 4.5 GHz (2.6 GHz) for Y3 (Y5); a 5 GHz discrepancy in the true band center would introduce a $\sim 5\%$ error on the NET values reported below. Lacking spectroscopy measurements for Y4b, we assume it to be similar to Y3, which is closer to the target band, rather than Y5.

5.2 Stop Mode Noise

During the flight, we took several short data sets with the payload in “stop mode,” where the pointing controls maintain the payload’s attitude in one direction. While the payload is in stop mode, the $1/f$ knee from scan-synchronous noise is suppressed, and the baseline detector performance can be evaluated more easily. These stop mode data sets were acquired during the first 24 hours at float, between initial system tests that required the antennas to be powered on. The usable times where the antennas were off amount to a ~ 115 minute dataset.

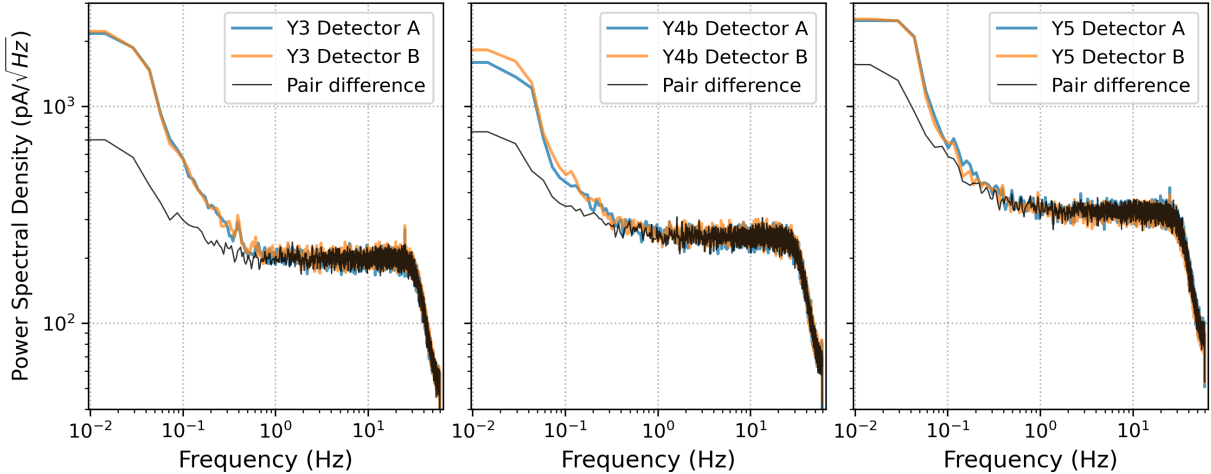


Figure 7: Power spectral density pair-difference plots from representative detector pairs on each FPU. The PSDs shown are the average of the PSDs calculated at each time chunk. The low-frequency correlated noise in the PSDs of the pair-difference time streams is suppressed.

5.2.1 Noise Power Spectral Density

The time-ordered data (TOD) used in the noise analysis is divided into smaller chunks and cleaned before calculating the detectors’ power spectral density (PSD). We apply flags to remove intermittent antenna pings and abnormal detector performance and stitch together large discontinuities (“flux jumps”). We divide the full TOD into chunks of 2^{13} samples, each ~ 68 seconds long. Any chunk with a flagged data fraction higher than 80% is excluded from the analysis. Finally, we remove a linear fit to each chunk, gap-fill the flagged regions with white noise of the same level as surrounding data, and compute the PSD.

Figure 7 shows representative noise PSDs from each of the three FPUs, expressed in units of equivalent TES current per square root bandwidth — the noise equivalent current (NEI). For each FPU, we plot PSDs for one detector pair (called A and B channels) and their difference $((A - B)/\sqrt{2})$. The plotted PSDs are averages from all stop-mode time chunks. The noise level on the 280 GHz bolometers is reasonably flat across frequencies between the $1/f$ knee (~ 0.4 Hz) to the roll-off at 30 Hz from the internal MCE digital filter. The majority of detectors have a low level of correlated noise resulting from temperature and loading drifts and some small, unresolved steps in the time streams. In the pair-difference PSD, the effects of the low-frequency correlated noise are suppressed. For the majority of detectors, the white noise levels between 0.5 and 3 Hz also show slight improvement; the median detector NEI decreases by 2.6%, 4.0%, and 1.0% for the Y3, Y4b, and Y5 arrays, respectively. A few readout columns exhibited intermittent, highly correlated electrical noise during flight, often presenting as frequent small jumps in the time streams. About 6% of detectors on each array are affected. The improvement in white noise levels in the pair-difference analysis on these columns is more drastic: 24%, 62%, and 32% for Y3, Y4b, and Y5, respectively. While the pair-difference analysis would reduce correlated noise, we choose to present results from the single-detector noise analysis below.

The estimate of each detector’s noise level in the stop mode analysis is derived from the median white noise value across all time chunks. We calculate the white noise level during each time chunk from the mean of the PSD between 0.5 and 3 Hz. This frequency range roughly covers the few-degree angular scale of interest for SPIDER’s beam size and scanning speed. The typical scanning speed during flight was 2.5 degrees per second, so the degree-scale signal drops off around 2.5 Hz.

5.2.2 Noise and Absorbed Optical Power

The photon noise contribution to total power on a polarized bolometer is expected to scale with absorbed optical power as

$$\text{NEP}_\gamma^2 = 2h\nu_0 P_{opt} + 2P_{opt}^2 / \Delta\nu, \quad (5)$$

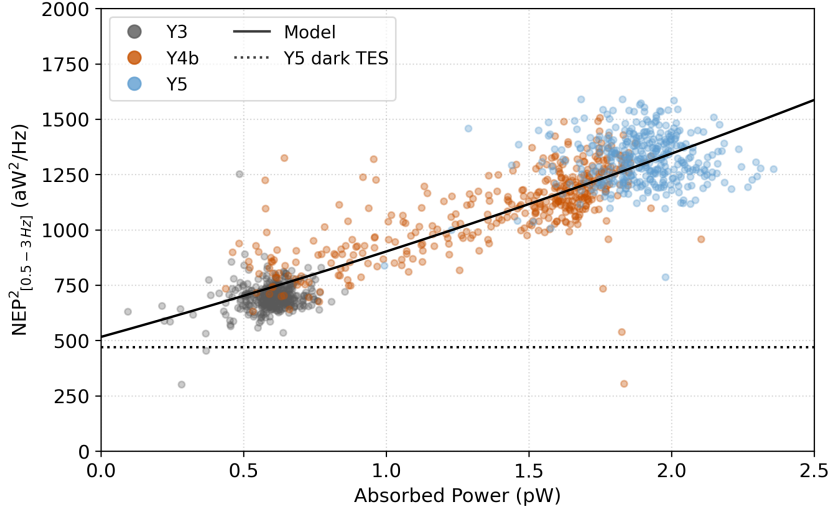


Figure 8: Median measured NEP^2 versus absorbed power P_{opt} , colored by receiver. The solid black line represents a model of the expected photon noise NEP^2 per absorbed power for a detector with band center and bandwidth matching the average Y3 and Y5 bandpass ($[\nu_0, \Delta\nu] = [270, 71 \text{ GHz}]$) with an offset fitted to the data to represent other detector noise contributions (e.g., amplifier noise and thermal fluctuation noise). The Y5 dark TES noise level is shown for comparison; the dark TES was biased low on its superconducting transition ($\sim 0.2 R_N$) during science data acquisition but nonetheless shows good agreement with the fitted offset. Detectors with excess correlated electrical noise have been omitted from the plot for clarity.

where ν_0 is the band center and $\Delta\nu$ is the bandpass. In SPIDER’s regime, the first term is expected to dominate. The spread in optical efficiencies, and thus the spread in P_{opt} , of the 280 GHz detectors allows us to demonstrate the dependence of bolometer noise on absorbed optical power.

In Figure 8, we plot the median noise level (NEP^2) against absorbed power for each of the 280 GHz detectors. The absorbed power is derived using the in-flight load curves (Figure 6a). We fit the data to a simple model: $\text{NEP}_{\text{Tot}}^2 = \text{NEP}_\gamma^2 + \text{offset}$. We model NEP_γ^2 as a detector with the average bandpass measurements of Y3 and Y5 ($\nu_0=270 \text{ GHz}$, and $\Delta\nu=71 \text{ GHz}$). The fitted offset closely matches the dark TES noise levels on Y5, which should reflect all non-optical noise sources in the bolometers and readout chain, such as amplifier noise and thermal fluctuation noise. We attribute any noise in excess of the offset/dark TES noise to photon noise. For this comparison, a small fraction (6%) of detectors from columns with highly correlated electrical noise are masked. The remaining data agree with photon noise-limited performance for the high-efficiency detectors.

5.2.3 280 GHz Instantaneous Sensitivity

The left-hand side of Figure 9 shows histograms of the single-detector median NET, estimated using the calibration described in Section 5.1. The achieved sensitivity on Y5 and the high-optical efficiency detectors on Y4b cluster around $350 \mu\text{K}_{\text{CMB}}\sqrt{s}$, whereas the extra neutral density filter on Y3 suppresses that array’s sensitivity. The median detector NET on Y3, Y4b, and Y5 are 624, 398, and $316 \mu\text{K}_{\text{CMB}}\sqrt{s}$, respectively; considering just the Y4b detectors with optical efficiency above 30%, that array’s median drops to $372 \mu\text{K}_{\text{CMB}}\sqrt{s}$.

The right-hand side of Figure 9 shows a cumulative plot of the total NET (NET_{Tot}) for all 280 GHz detectors. The data are grouped by FPU and sorted from least to most sensitive. The FPU sensitivity for Y5 alone is $\sim 15 \mu\text{K}_{\text{CMB}}\sqrt{s}$. This exceptional performance results from Y5’s high yield, high optical efficiency, and low noise, surpassing the proposal-level forecast of $18 \mu\text{K}_{\text{CMB}}\sqrt{s}$ (per receiver) in Ref. 3. Although Y4b and Y3 are moderately less sensitive, all three receivers individually exhibit better instantaneous NET than any previously published result above 220 GHz. The combined 280 GHz sensitivity is $\sim 11.2 \mu\text{K}_{\text{CMB}}\sqrt{s}$, which is on par with the forecast total sensitivity in Fraisse et al. 2013 ($\sim 10.5 \mu\text{K}_{\text{CMB}}\sqrt{s}$).³

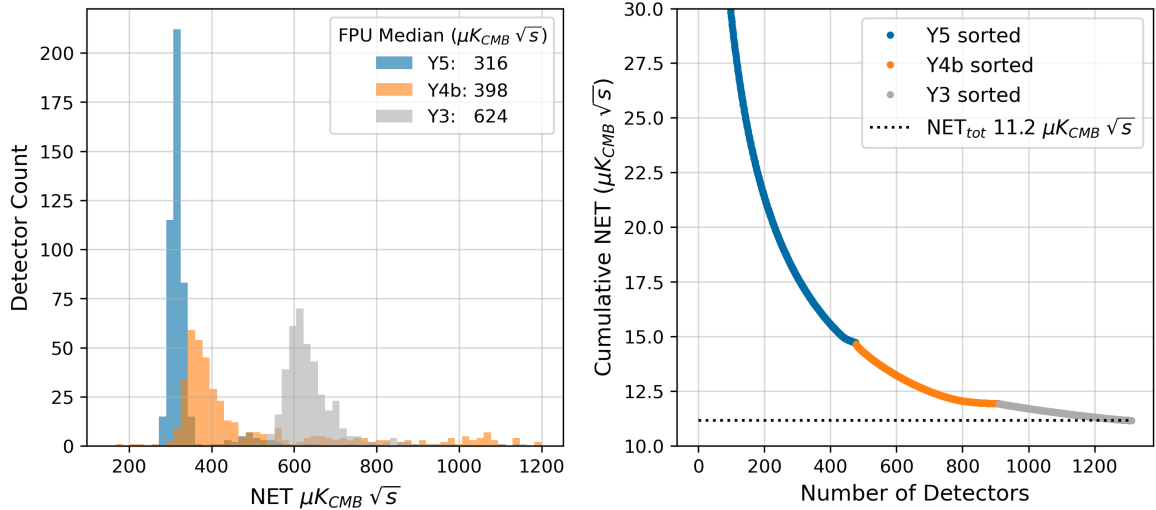


Figure 9: (*Left*): Histogram of median detector NET colored by focal plane for all stop-mode data. (*Right*): Cumulative NET for all 280 GHz detectors. The data are grouped by FPU and sorted from least to most sensitive. The overlap of detector sensitivity between FPUs results in cusps in the cumulative NET curve. The black dotted line marks the total sensitivity.

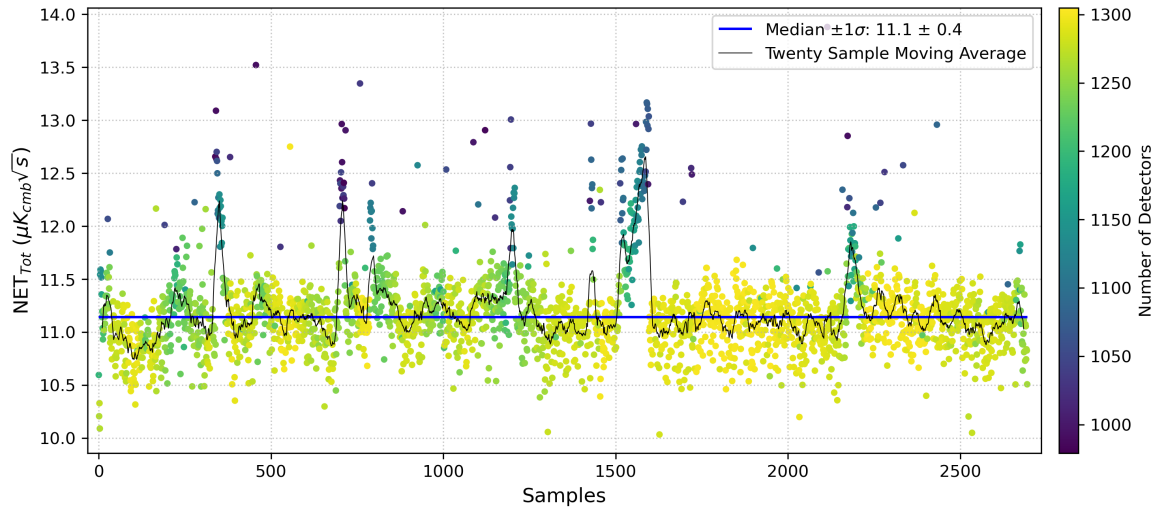


Figure 10: 280 GHz NET_{Tot} for a very conservatively flagged subset of scanning data during flight. Each data point represents ~ 1 minute of data and is colored by the number of detectors included in the NET_{Tot} calculation. The black line is a moving average of the data samples, and the horizontal line marks the median value. We find similar baseline noise performance in the scanning data as in the stop mode data.

5.3 Full-Flight Scanning Noise

In this section, we extend the noise analysis to a subset of the science scanning data. During the data selection, we subdivide the TOD into 2^{13} sample-long chunks and apply very strict and conservative flagging and time stream cleaning. We exclude time chunks in which more than 25% of nominally live detectors are flagged. The remaining data, when combined, is approximately 51 hours long. To address larger scan-synchronous signals, we apply a third-order polynomial filter and report the average white noise levels between 2 and 4 Hz. We then evaluate NET_{Tot} using all unflagged 280 GHz detectors for each ~ 1 minute-long chunk. Figure 10 shows the behavior in NET_{Tot} for the 51-hour dataset, where the data is colored by the number of detectors used in the cumulative sum. The median NET_{Tot} across the dataset is $11.1 \pm 0.4 \mu\text{K}_{\text{CMB}}\sqrt{s}$ —similar to the stop-mode

dataset. The larger fluctuations in sensitivity shown in the figure correlate strongly with higher detector flagging fractions from events like fridge cycles or, in some cases, sub-optimal detector biasing. One instance of increased NET_{Tot} , around sample 1500, is from a brief interruption in the bias tracking algorithm on the Y5 FPU. The smaller variations in NET_{Tot} are likely due to fluctuations in the cryogenic temperatures and optical loading on the TESs, as discussed in Section 4. The cryogenic temperatures fluctuated during the first half of the scanning mode dataset but were more stable in the second half; the trend in NET_{Tot} follows a similar pattern. However, we leave a more detailed review of those features for a future publication. Overall, the baseline performance demonstrates the stability of the balloon platform for CMB observations.

We emphasize that these are only preliminary estimates on NET. The absolute calibration for SPIDER’s science analysis will be derived by cross-calibrating degree-scale power in our maps against *Planck*’s maps of the CMB temperature anisotropies.⁶

6. CONCLUSION

The SPIDER CMB experiment has completed its second and final NASA Long Duration Balloon flight and mapped the Southern skies in three frequency bands: 95, 150, and 280 GHz. The three novel 280 GHz receivers deployed during the second flight were the first implementations of the NIST feedhorn-coupled TES array technology at 280 GHz and the first to use the technology for observations from a balloon. The detectors and receivers performed exceptionally during the flight, demonstrating low photon loading and good noise performance at 280 GHz. The preliminary noise analysis presented here (not calibrated against the CMB) shows the best achieved combined NET for the 280 GHz instrument to be near $11.2 \mu\text{K}_{\text{CMB}}\sqrt{s}$. We expect that the resulting maps at 280 GHz will obtain a higher signal-to-noise on Galactic dust than any currently available in this sky region and will provide lasting value to the field.

ACKNOWLEDGMENTS

SPIDER is supported in the U.S. by NASA under grants NNX07AL64G, NNX12AE95G, NNX17AC55G, and 80NSSC21K1986 issued through the Science Mission Directorate, and by the National Science Foundation through PLR-1043515. Logistical support for the Antarctic deployment and operations is provided by the NSF through the U.S. Antarctic Program. Recovery of the SPIDER-2 data and hardware was led by personnel from Columbia Scientific Balloon Facility, Antarctic Service Contract, SPIDER, Kenn Borek Air, and South Pole Station. Support in Canada is provided by the Natural Sciences and Engineering Research Council and the Canadian Space Agency. Support in Norway is provided by the Research Council of Norway. The Dunlap Institute is funded through an endowment established by the David Dunlap family and the University of Toronto. The Flatiron Institute is supported by the Simons Foundation. JEG acknowledges support from the Swedish Research Council (Reg. no. 2019-03959) and the Swedish National Space Agency (SNSA/Rymdstyrelsen). We acknowledge the use of Grammarly in the final proofreading of this document.

REFERENCES

- [1] Filippini, J. P. et al., “SPIDER: a balloon-borne CMB polarimeter for large angular scales,” *Proc. SPIE* **7741** (2010).
- [2] Ade, P. A. R. et al., “Antenna-coupled TES bolometers used in BICEP2, Keck Array, and SPIDER,” *ApJ* **812**, 176 (10 2015).
- [3] Fraisse, A. A. et al., “SPIDER: probing the early universe with a suborbital polarimeter,” *J. Cosmol. Astropart. P.* **2013**, 047–047 (4 2013).
- [4] Gualtieri, R. et al., “SPIDER: CMB Polarimetry from the Edge of Space,” *J. Low Temp. Phys.* **193**, 1112–1121 (Dec 2018).
- [5] The Planck Collaboration, “Planck 2018 results. iv. diffuse component separation,” *A&A* **641**, A4 (Sept. 2020).

- [6] SPIDER Collaboration, Ade, P. A. R., Amiri, M., Benton, S. J., Bergman, A. S., Bihary, R., Bock, J. J., Bond, J. R., Bonetti, J. A., Bryan, S. A., Chiang, H. C., Contaldi, C. R., Doré, O., Duivenvoorden, A. J., Eriksen, H. K., Farhang, M., Filippini, J. P., Fraisse, A. A., Freese, K., Galloway, M., Gambrel, A. E., Gandilo, N. N., Ganga, K., Gualtieri, R., Gudmundsson, J. E., Halpern, M., Hartley, J., Hasselfield, M., Hilton, G., Holmes, W., Hristov, V. V., Huang, Z., Irwin, K. D., Jones, W. C., Karakci, A., Kuo, C. L., Kermish, Z. D., Leung, J. S. Y., Li, S., Mak, D. S. Y., Mason, P. V., Megerian, K., Monceli, L., Morford, T. A., Nagy, J. M., Netterfield, C. B., Nolta, M., O’Brien, R., Osherson, B., Padilla, I. L., Racine, B., Rahlin, A. S., Reintsema, C., Ruhl, J. E., Runyan, M. C., Ruud, T. M., Shariff, J. A., Shaw, E. C., Shiu, C., Soler, J. D., Song, X., Trangsrud, A., Tucker, C., Tucker, R. S., Turner, A. D., van der List, J. F., Weber, A. C., Wehus, I. K., Wen, S., Wiebe, D. V., and Young, E. Y., “A constraint on primordial b-modes from the first flight of the spider balloon-borne telescope,” *ApJ* **927**, 174 (March 2022).
- [7] SPIDER Collaboration, Ade, P. A. R., Amiri, M., Benton, S. J., Bergman, A. S., Bihary, R., Bock, J. J., Bond, J. R., Bonetti, J. A., Bryan, S. A., Chiang, H. C., Contaldi, C. R., Doré, O., Duivenvoorden, A. J., Eriksen, H. K., Filippini, J. P., Fraisse, A. A., Freese, K., Galloway, M., Gambrel, A. E., Gandilo, N. N., Ganga, K., Gourapura, S., Gualtieri, R., Gudmundsson, J. E., Halpern, M., Hartley, J., Hasselfield, M., Hilton, G., Holmes, W., Hristov, V. V., Huang, Z., Irwin, K. D., Jones, W. C., Karakci, A., Kuo, C. L., Kermish, Z. D., Leung, J. S. Y., Li, S., Mak, D. S. Y., Mason, P. V., Megerian, K., Monceli, L., Morford, T. A., Nagy, J. M., Netterfield, C. B., Nolta, M., O’Brien, R., Osherson, B., Padilla, I. L., Racine, B., Rahlin, A. S., Reintsema, C., Ruhl, J. E., Runyan, M. C., Ruud, T. M., Shariff, J. A., Shaw, E. C., Shiu, C., Soler, J. D., Song, X., Trangsrud, A., Tucker, C., Tucker, R. S., Turner, A. D., van der List, J. F., Weber, A. C., Wehus, I. K., Wiebe, D. V., and Young, E. Y., “Analysis of polarized dust emission from the first flight of the spider balloon-borne telescope,” (2024).
- [8] Runyan, M. C. et al., “Design and performance of the spider instrument,” *Proc. SPIE* **7741** (2010).
- [9] Rahlin, A. S. et al., “Pre-flight integration and characterization of the SPIDER balloon-borne telescope,” *Proc. SPIE* **9145** (2014).
- [10] Rahlin, A. S., *The First Flight of the SPIDER Balloon-Borne Telescope*, PhD thesis, Princeton University (2016).
- [11] Nagy, J. M., *Optical Development for the SPIDER Balloon-Borne CMB Polarimeter*, PhD thesis, Case Western Reserve University (2016).
- [12] Tucker, R. S., *Characterization of Detectors and Instrument Systematics for the SPIDER CMB Polarimeter*, PhD thesis, California Institute of Technology (2014).
- [13] Leung, J. S.-Y., *From the Ends of the Earth to the Edge of the Universe: New Tools for Overcoming the Extreme Environments of CMB Experiments*, PhD thesis, University of Toronto (2023).
- [14] Li, S., *Optomechanical Optimizations for Balloon-borne Telescopes*, PhD thesis, Princeton University (2023).
- [15] Gudmundsson, J. E. et al., “The thermal design, characterization, and performance of the spider long-duration balloon cryostat,” *Cryogenics* **72**, 65–76 (12 2015).
- [16] Song, X., *Integration and Analysis of the Balloon-borne Telescope, SPIDER*, PhD thesis, Princeton University (2022).
- [17] Bergman, A. S., *Commissioning the SPIDER-2 instrument and SPIDER-1 low level analysis*, PhD thesis, Princeton University (2019).
- [18] Shaw, E. C. et al., “Design and pre-flight performance of SPIDER 280 ghz receivers,” *Millimeter, Submillimeter, and Far-Infrared Detectors and Instrumentation for Astronomy X* **114532** (2020).
- [19] Shaw, E. C., *280 GHz receivers for the SPIDER CMB polarimeter*, PhD thesis, University of Illinois Urbana-Champaign (2023).
- [20] Hubmayr, J. et al., “Design of 280 ghz feedhorn-coupled TES arrays for the balloon-borne polarimeter SPIDER,” *Proc. SPIE* **9914** (2016).
- [21] de Korte, P. A. J., Beyer, J., Deiker, S., Hilton, G. C., Irwin, K. D., MacIntosh, M., Nam, S. W., Reintsema, C. D., Vale, L. R., and Huber, M. E., “Time-division superconducting quantum interference device multiplexer for transition-edge sensors,” *Review of Scientific Instruments* **74**, 3807–3815 (07 2003).
- [22] Battistelli, E. et al., “Functional description of read-out electronics for time-domain multiplexed bolometers for millimeter and sub-millimeter astronomy,” *J. Low Temp. Phys.* **151**, 908–914 (2008).

- [23] Bryan, S. A. et al., “Modeling and characterization of the SPIDER half-wave plate,” *Proc. SPIE* **7741** (2010).
- [24] Bryan, S., Ade, P., Amiri, M., Benton, S., Bihary, R., Bock, J., Bond, J. R., Chiang, H. C., Contaldi, C., Crill, B., and et al., “A cryogenic rotation stage with a large clear aperture for the half-wave plates in the spider instrument,” *Review of Scientific Instruments* **87**, 014501 (1 2016).
- [25] Tucker, C. E. and Ade, P. A. R., “Thermal filtering for large aperture cryogenic detector arrays,” in [*Millimeter and Submillimeter Detectors and Instrumentation for Astronomy III*], Zmuidzinas, J., Holland, W. S., Withington, S., and Duncan, W. D., eds., **6275**, 62750T, International Society for Optics and Photonics, SPIE (2006).
- [26] Ade, P. A. R., Pisano, G., Tucker, C., and Weaver, S., “A review of metal mesh filters,” in [*Millimeter and Submillimeter Detectors and Instrumentation for Astronomy III*], Zmuidzinas, J., Holland, W. S., Withington, S., and Duncan, W. D., eds., **6275**, 62750U, International Society for Optics and Photonics, SPIE (July 2006).
- [27] Halpern, M., Gush, H., Wishnow, E., and De Cosmo, V., “Far infrared transmission of dielectrics at cryogenic and room temperatures: glass, fluorogold, eccosorb, stycast, and various plastics,” *Applied optics* **25**, 565 (03 1986).
- [28] Gambrel, A. E., *Measurement of the Polarization of the Cosmic Microwave Background with the SPIDER Instrument*, PhD thesis, Princeton University (2018).
- [29] Irwin, K. and Hilton, G., [*Transition-Edge Sensors*], 63–150, Springer Berlin Heidelberg, Berlin, Heidelberg (2005).